buildings

MDPI

Article

Study on the Physical, Mechanical, Microscopic and Durability Properties of Artificial Aggregate from Waste Travertine Powder

Tianzhen Li [1], Yichen Feng [2], Kaiyang Wang [3], Xiaonan Tang [2], Jun Xia [2], Chao Zhang [1], Xueyang Miao [1], Bin Xi [4,5,*] and Mengdi Liu [6,*]

1 College of Mechanical and Electronic Engineering, Nanjing Forestry University, Nanjing 210037, China; tianzhen.li@njfu.edu.cn (T.L.); chaozhang@njfu.edu.cn (C.Z.); xymiao@njfu.edu.cn (X.M.)
2 Department of Civil and Environmental Engineering, The University of Liverpool, Liverpool L69 3BX, UK; yichenfeng001@163.com (Y.F.); xiao.tang@xjtlu.edu.cn (X.T.); jun.xia@xjtlu.edu.cn (J.X.)
3 Department of Construction Management, Nanjing Forestry University, Nanjing 210037, China; kaiyang.wang@njfu.edu.cn
4 School of Mechanics and Construction Engineering, Jinan University, Guangzhou 510632, China
5 Key Laboratory of Marine Civil Engineering Materials and Structures, Ministry of Education of China, Guangzhou 510632, China
6 School of Management Science and Engineering, Shandong Technology and Business University, Yantai 264005, China
* Correspondence: bin.xi@polimi.it (B.X.); 202414306@sdtbu.edu.cn (M.L.)

Abstract

To promote the resource utilization of travertine waste and alleviate the shortage of natural aggregates, artificial aggregates were prepared by cold-bonding granulation using 70% waste travertine powder as the main raw material and 30% binders (cement, fly ash, and GGBS). Four binder systems were designed: a pure cement system, a cement–fly ash binary system, and two cement–fly ash–GGBS ternary systems. The effects of the binder system on the physical properties, mechanical properties, microstructure, and freeze-thaw durability were investigated. Results showed that the binder system clearly influenced aggregate performance. In the pure cement system (G1), sufficient hydration products produced a denser internal structure and better freeze-thaw resistance. The cylindrical and particle compressive strengths reached 6.23 MPa and 3.04 MPa respectively, and the mass loss rate after 25 freeze–thaw cycles was only 2.27%. With fly ash, the delayed early pozzolanic reaction resulted in a more porous structure and inferior overall performance. The strength loss of G2 was nearly half that of G1, while higher porosity and water absorption rates were observed. The addition of GGBS promoted additional gel formation through latent hydraulic reactions, enhancing pore filling and structural densification and thus improving overall performance. G4, with higher GGBS content, performed better: its cylindrical and particle compressive strengths were 34% and 39% higher than those of G2, respectively; its water absorption and porosity were 16% and 21% lower than those of G2, respectively. These results confirm that high-content travertine powder artificial aggregates can be feasibly produced using a cement–fly ash–GGBS multi-component cementitious system, offering a sustainable route for travertine waste utilization and environmental benefits.

Keywords: artificial aggregate; waste travertine powder; solid waste utilization; cementitious system; environmental benefits

Academic Editor: Antonio Caggiano

Received: 10 October 2026
Revised: 18 November 2026
Accepted: 18 November 2026
Published: 20 November 2026

Copyright: © 2026 by the authors. Licensee MDPI, Basel, Switzerland. This article is an open access article distributed under the terms and conditions of the Creative Commons Attribution (CC BY) license.

1. Introduction

The resource recovery of solid waste is crucial for achieving global carbon reduction goals and sustainable development. With the continuous generation of massive amounts of industrial and construction waste worldwide, international researchers are actively exploring the utilization of industrial by-products and construction demolition waste to produce sustainable building materials [1–3]. It is highly imperative to enhance the comprehensive utilization level of solid waste and promote the application of recycled materials on a global scale. As a key component of concrete, the extraction and processing of aggregates impose additional environmental burdens, including land disturbance, ecosystem damage, and transportation-related carbon emissions [4]. According to relevant research statistics, the global construction industry extracts approximately 40 billion metric tons of sand and gravel annually [5]; the extraction volume of natural aggregates is huge but is gradually depleting. As natural resources continue to be depleted and an ever-increasing volume of solid waste is generated, producing artificial aggregates using industrial solid waste or construction debris has become a critical research problem in the utilization of resources for construction materials [6–8]. Artificial aggregates not only partially replace natural aggregates, thereby alleviating pressure on resource extraction, but also enable the high-value utilization of solid waste, potentially offering environmental benefits and promising prospects for engineering applications [9]. However, a quantitative life-cycle assessment (LCA) is beyond the scope of this study, and the environmental benefits should be validated through systematic LCA in future work.

Travertine is a type of sedimentary rock mainly composed of calcium carbonate ($CaCO_3$) [10]. Due to its uniform texture, moderate hardness, and ease of processing, it is widely used in exterior walls and interior decoration. However, the mining, cutting, processing, and demolition of travertine structures generate large amounts of waste powder and scrap [11]. If these wastes are disposed of through the traditional landfill method, it will not only easily cause environmental problems, but also consume land resources [10,12]. Therefore, recycling waste travertine powder as a raw material for construction materials holds potential environmental value and engineering significance [13]. Unlike highly reactive solid wastes (e.g., fly ash or GGBS), carbonate-based waste materials such as travertine powder are generally considered relatively inert fillers. Their addition can alter the pore structure and provide nucleation sites, but may also dilute the cementitious matrix, potentially affecting the long-term durability of the resulting composites [10,13]. Based on this, this paper attempts to incorporate travertine powder into an artificial aggregate production system, with the aim of reusing waste stone resources and thereby reducing the environmental impact of construction waste.

Among the methods for preparing artificial aggregates, cold-bonding granulation technology has received widespread attention due to its simple process, low energy consumption, and suitability for the resource recovery of powdered solid waste [14]. Under ambient temperature conditions, this technology utilizes the physical bonding and chemical cementation effects of the adhesive to cause fine particles to gradually agglomerate and form granular bodies with a certain strength [14]. Compared to high-temperature sintering or steam curing, cold-bonding granulation is more energy-efficient but often results in higher initial porosity and lower early strength. Consequently, the durability of cold-bonded aggregates (e.g., freeze-thaw resistance and water absorption) remains a critical challenge and is highly dependent on the densification of the binder matrix. In the early stages of granulation, water forms liquid bridges between particles and generates capillary forces, promoting nucleation and agglomeration of the powder. Subsequently, through rolling and encapsulation, as well as continuous hydration, the particles gradually grow and become denser. At the same time, hydration products such

as C-S-H gel transform the initial physical bonds between powder particles into a more stable chemical cementation structure, thereby imparting the necessary mechanical properties to the aggregate [15].

Previous studies have explored various solid wastes for artificial aggregates, but their findings revealed distinct differences based on the waste type and binder system. For highly reactive solid wastes (e.g., fly ash and GGBS), the main strategy is to promote pozzolanic reactions. For instance, Narattha and Chaipanich [16] utilized high-calcium fly ash with cement and calcium hydroxide to achieve synergistic hydration. Similarly, Pan et al. [17] and Zhang et al. [18] both demonstrated that introducing multicomponent binder systems (e.g., fly ash combined with GGBS) can form more C-S-H gels, significantly enhancing the cylindrical compressive strength. However, Zhang et al. [18] noted that while a 70% fly ash system with 15% GGBS yields high strength, the durability (e.g., freeze-thaw resistance) under harsh environments still requires careful optimization. In contrast to these silicate-based systems, Ma et al. [19] and Shang et al. [20] focused on alkaline or carbonate-rich environments; Shang et al. [20] used CO_2 carbonation to densify concrete slurry aggregates, proving that carbonate precipitation can effectively reduce water absorption. Compared with these studies, the utilization of travertine powder faces a unique challenge: travertine is a carbonate-based waste material with low hydraulic reactivity. While Shang et al. [20] demonstrated that carbonation can improve density, relying solely on travertine powder may lead to a loose internal pore structure. Therefore, understanding how multicomponent binder systems interact with high-content carbonate waste to enhance both mechanical strength and durability is crucial. Tian et al. [21] also highlighted that uniform pore distribution and particle bonding are key to structural integrity in red mud systems, indicating that the physical and chemical synergy between the filler (like travertine powder) and the binder matrix is more critical than the absolute strength of individual components.

Although these studies have demonstrated the feasibility of utilizing various solid wastes, most have focused primarily on mechanical strength. Systematic investigations into how multicomponent binder systems (e.g., OPC–FA–GGBS) influence the pore structure, microstructural evolution, and durability of carbonate-rich artificial aggregates remain lacking. Furthermore, the synergistic mechanisms among these components require more critical evaluation. Existing research on travertine waste has primarily focused on the preparation of geopolymers [22], artificial stone [23], and concrete [12,24]. However, research on artificial aggregate production using travertine powder is still limited. In particular, artificial aggregates prepared with high-content travertine powder as the main raw material still face issues such as insufficient early-age hydration activity, a loose internal pore structure, and limited strength development. Furthermore, the mechanisms by which materials such as fly ash and GGBS interact chemically and physically with high-content waste travertine powder to produce synergistic effects, as well as the mechanisms governing the microstructural evolution of artificial aggregates, remain unclear. Systematic research on the mechanisms of densification involving multiple cementitious materials in systems with high-content travertine powder is still relatively insufficient.

Therefore, this paper prepared artificial aggregates using cement, fly ash, GGBS, and high-content travertine powder as the main raw materials, and conducted research on the factors influencing the properties of the aggregate. First, a research system for artificial aggregates was established using a high-content waste travertine powder (70%) combined with low-content cementitious materials (30%). Second, a comparative research system was established, comprising a "reference system (cement:travertine powder), a binary synergistic series (cement:fly ash:travertine powder), and a ternary syner-

gistic series (cement:fly ash:GGBS:travertine powder).” The patterns of change in the macroscopic and microscopic properties of the artificial aggregate under different dosages of active cementitious materials were analyzed and the mechanism of densification through the synergistic use of multiple solid waste materials was elucidated, which provided a basis for the preparation of artificial aggregate and the resource recovery of travertine waste.

2. Methodology

2.1. Materials

The P.O 52.5 ordinary Portland cement (OPC), Class I fly ash (FA), S95 granulated blast furnace slag powder (GGBS), and waste travertine powder (TP) were used in this study as the primary raw materials, as shown in Figure 1. Among these, cement served as the primary cementing material, fly ash and GGBS as auxiliary cementing materials, and travertine powder as the primary solid waste raw material. Figure 2 shows the the particle-size distribution, and the particle size of the travertine powder was less than 300 μm. All raw materials were pretreated prior to use to ensure that their particle size and condition met the experimental requirements. Figure 3 shows the scanning electron microscope (SEM) images of the travertine. The X-ray diffraction (XRD) pattern of the travertine powder is shown in Figure 4. The main chemical components of cement, fly ash, GGBS and travertine powder were determined by X-ray fluorescence (XRF) spectroscopy, as shown in Table 1. In this study, tap water was used as the mixing water [25,26].



Figure 1. Raw materials for the travertine artificial aggregate.

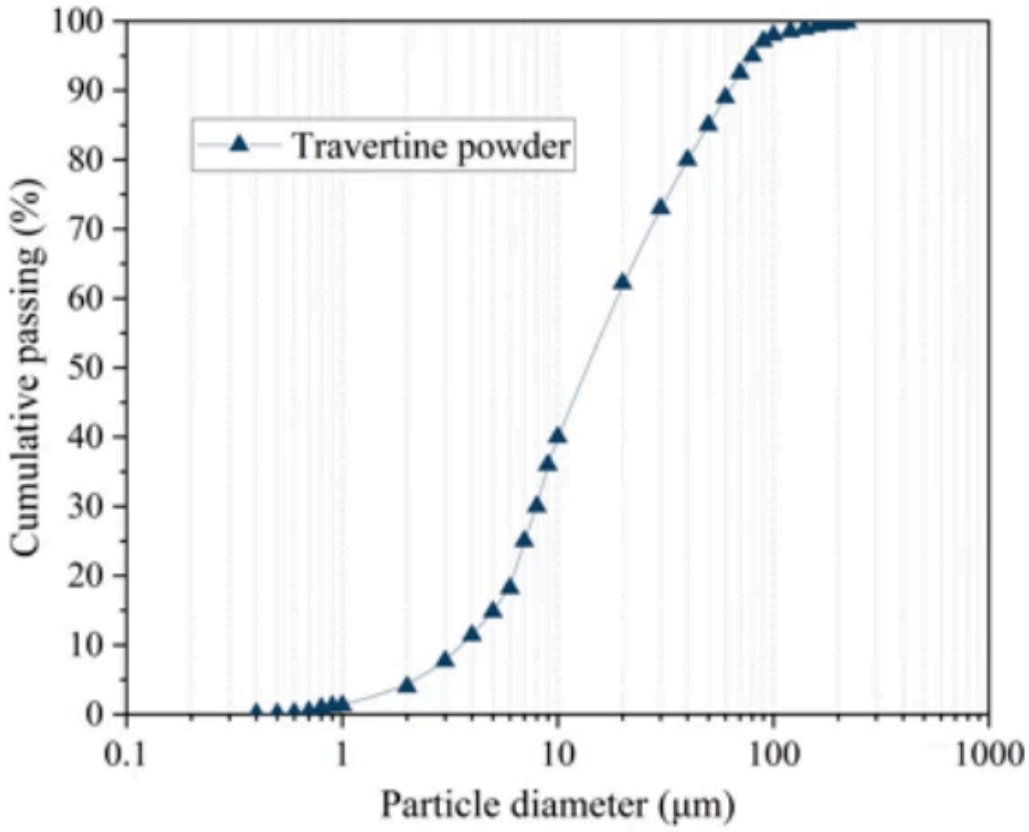


Figure 2. Size distribution of the travertine powder.

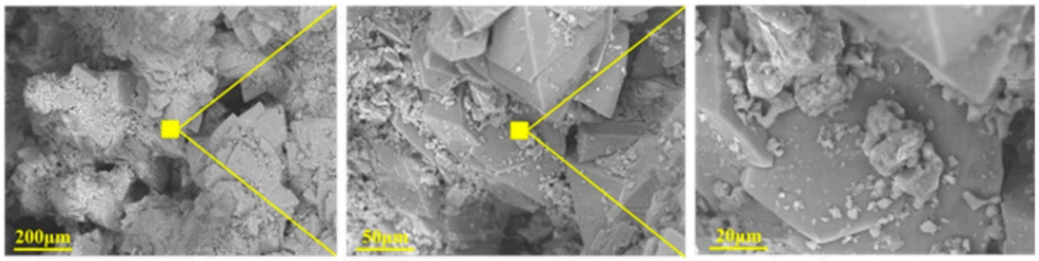


Figure 3. SEM image of travertine.

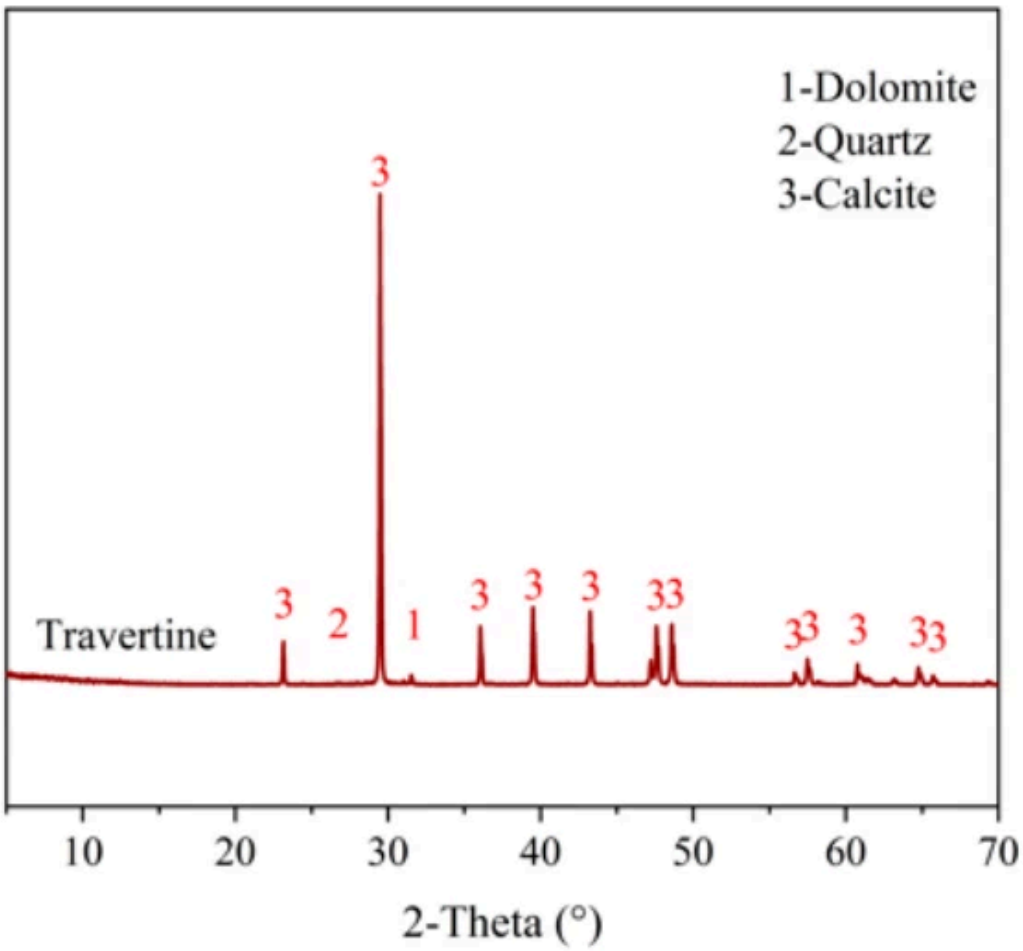


Figure 4. XRD image of travertine.

Table 1. Main chemical components of cement, fly ash, GGBS and travertine (wt%).

Material	CaO	SiO_2	Al_2O_3	MgO	Fe_2O_3	P_2O_5	SO_3	SrO	K_2O	TiO_2	LOI
Cement	59.50	22.48	5.76	3.17	3.41	-	2.60	0.10	0.72	0.33	3.45
Fly ash	3.70	47.70	37.53	0.94	4.55	0.36	-	0.10	1.62	1.40	4.32
GGBS	36.82	26.75	19.66	11.10	0.32	-	2.65	-	0.29	0.94	0.41
Travertine	55.04	1.18	0.46	0.35	0.18	0.16	0.13	0.10	0.06	0.05	42.26

2.2. Mix Proportions and Specimen Preparation

To determine the optimal values for water/solid ratio (w/s, defined as the mass ratio of water to the total solid mass of travertine powder and binder) and granulation time during the preparation of the travertine artificial aggregate, this study first selected a mixture ratio of 70% travertine powder (TP) and 30% cementitious material for parameter optimization. This cementitious material group consisted solely of cement; its simple composition facilitated an accurate assessment of the influence of the w/s and granulation time on the forming results and mechanical properties without interference from variables such as fly ash (FA) or GGBS. A total of four sets of samples were prepared, with the w/s ratio set at intervals of 0.02 within the range of 0.13–0.19. These samples were systematically evaluated based on key indicators such as pelletization effectiveness, apparent integrity, forming stability, and early strength. The results indicated that the aggregate exhibited good forming performance when the w/s ratio was between 0.15

and 0.19 and the granulation time was 14 min. Considering the potential requirements for formability, strength properties, and durability comprehensively, the w/s was ultimately set at 0.15 and the granulation time at 14 min for all mix ratio series in this study.

To maximize the resource utilization of waste travertine powder, the incorporation ratio of waste travertine powder in the preparation of the artificial aggregate was fixed at 70%, with the remaining 30% allocated to the binder. Four different binder systems were established to evaluate their impact on the macroscopic and microscopic properties, while the TP content (70%), total binder content (30%), w/s (0.15), and granulation time (14 min) were kept constant; only the binder composition was varied. Based on Shrestha's research, a reference system G1 (30% OPC + 70% TP) was established using pure cement as the sole cementitious material [27], in which OPC accounts for the entire 30% binder. In order to analyze the effect of partially replacing cement with fly ash, a binary system G2 (15% OPC + 15% FA + 70% TP) with a cement:fly ash ratio of 1:1 was established, in which 50% of the OPC was replaced by FA on an equal-mass basis. It should be noted that the G1–G2 comparison therefore reflects the combined effect of OPC reduction and FA introduction, rather than a pure FA effect. Li et al. indicated that concrete with high strength characteristics can be produced with a ratio of 10:9:1 for cement, fly ash and GGBS [28]; therefore, a corresponding ternary system G3 (15% OPC + 13.5% FA + 1.5% GGBS + 70% TP) was established. To further investigate the performance of the travertine artificial aggregate in a ternary system, group G4 (15% OPC + 10.5% FA + 4.5% GGBS + 70% TP) was established with a cement:fly ash:GGBS ratio of 10:7:3. In both G3 and G4, the OPC content was kept at 15% and the total content of FA + GGBS at 15%, so that GGBS progressively replaced FA at FA:GGBS ratios of 9:1 (G3) and 7:3 (G4). Consequently, the G2–G3–G4 sequence mainly isolates the effect of GGBS-for-FA substitution under a fixed OPC content, whereas comparisons between G1 and G3/G4 involve simultaneous changes in OPC, FA, and GGBS and should be interpreted as combined effects. The mix proportions and the design comparison purpose of each system are shown in Table 2.

Table 2. Mix design of the travertine artificial aggregate.

Group	Cement (wt%)	Fly Ash (wt%)	GGBS (wt%)	Travertine (wt%)	Cement (kg)	Fly Ash (kg)	GGBS (kg)	Travertine (kg)	w/s
G1	30	0	0	70	2.1	0	0	4.9	0.15
G2	15	15	0		1.05	1.05	0		
G3	15	13.5	1.5		1.05	0.945	0.105		
G4	15	10.5	4.5		1.05	0.735	0.315		

For each batch, the total solid mass was 7.0 kg (4.9 kg travertine powder and 2.1 kg binder). With a water content of 1.05 kg, the w/s ratio was calculated as 1.05/7.0 = 0.15. If calculated solely based on the binder mass, the water/binder (w/b) ratio would be 1.05/2.1 = 0.50, which was within the normal range for cementitious systems. However, because 70% of the solid is relatively inert travertine powder, the w/s ratio is also appropriate to reflect the granulation water demand in this study.

For experimental accuracy, the materials for each group were weighed using a precision balance under the same conditions. To ensure uniform mixing, the materials were mixed outside the granulator after weighing. The materials were stirred thoroughly until visually uniform, i.e., until the mixture had a consistent color with no noticeable local variations. Based on the granulator's capacity, 7 kg of raw materials for the travertine artificial aggregate was prepared for each production batch. Using a precision balance,

0.525 kg of water was weighed and poured into a pressurized spray bottle; subsequently, under the same conditions, the remaining 0.525 kg of water was weighed and poured into a beaker for later use. The artificial aggregate was prepared using a disc-type granulator (disc diameter: 1000 mm, disc depth: 220 mm), with the inclination angle set to 45° and the rotational speed set to 45 r/min. A scraper was fixed inside the disc to promote particle collision and densification.

During the test, the entire batch of pre-mixed dry material was poured into the granulation disc at once, and the timer was started when the equipment was activated. During the first 30 s, the materials were uniformly re-mixed under the combined action of centrifugal force and gravity. Within the first minute, 0.525 kg of mixing water was evenly sprayed onto the surface of the material in a mist form using a pressurized spray bottle. Subsequently, the remaining 0.525 kg of water was sprayed at a rate of 100 g every 2–3 min until pelletization was essentially completed. The entire granulation process was continued for 14 min before being stopped, at which point spherical aggregates had formed. After the equipment was shut down, the aggregates were carefully transferred to trays for preliminary curing for 24 h, followed by immersion in water for 28 days of standard curing. The entire process for preparing the artificial travertine aggregate is shown in Figure 5.

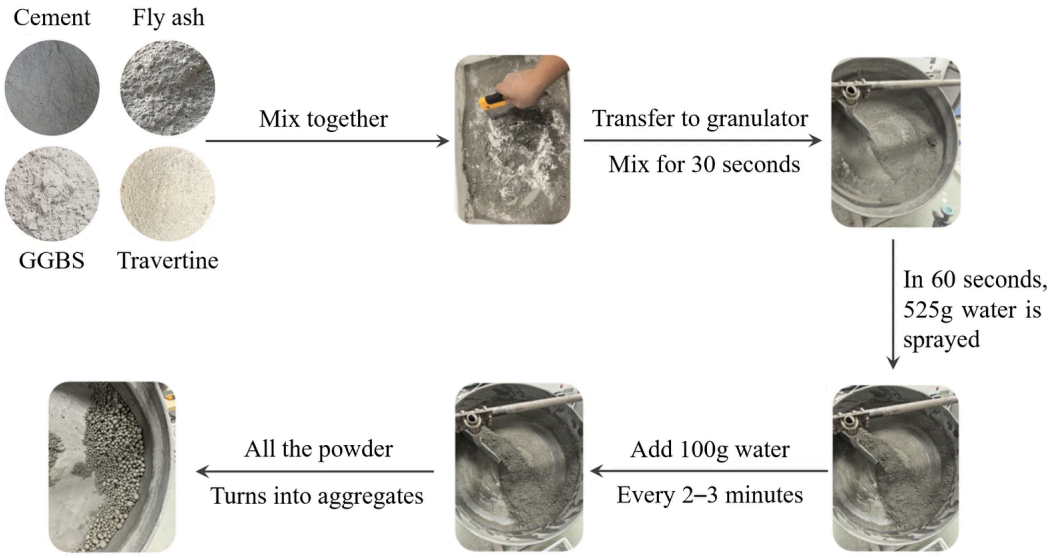


Figure 5. Production process of the travertine artificial aggregate.

2.3. Characterization Methods

For each mixing ratio, three independent production batches were prepared. Considering the total weight of each batch of samples, two sets of parallel test samples were randomly selected from each batch for independent testing. The representative value of each batch was the average of its two parallel specimens. The final results are reported as the mean ± standard deviation calculated from the three batch-averaged values. The prepared artificial aggregates were first used for non-destructive testing: aggregates with a particle size of 4.75–26.5 mm were used to determine the apparent density (each batch was tested twice in accordance with GB/T 14685-2011 [29]), while the 4.75–9.5 mm particle size portion recovered after the apparent density test was used to determine the porosity and water absorption rate. Both indicators were calculated based on the same saturated drying dataset. The 9.5–26.5 mm particle size portion was used to determine the bulk density. After completing the above non-destructive testing, the aggregates were dried to constant weight and then used for cylindrical compressive strength,

particle compressive strength, and freeze–thaw tests. Before freeze–thaw testing, the recovered aggregate was re-saturated. Due to the limited sample mass, destructive and freeze–thaw tests were conducted on the recovered aggregates from the non-destructive testing, rather than on separately sampled virgin aggregate.

2.3.1. Apparent Density

The apparent density test was developed based on GB/T 14685-2011 [29]. First, the specimens cured for 28 days were placed in a drying oven at 105 ± 5 °C until a constant weight was achieved. Fine particles smaller than 4.75 mm were removed using a standard sieve, and a 2 kg sample from the 4.75–26.5 mm size range was selected as the test specimen. After rinsing off surface dust, the sample was soaked in water for 24 h to reach a state of water saturation. Using a suspended electronic platform scale, the following measurements were taken in sequence: the total mass G_1 of the saturated, dried specimen (including the basket and specimen) submerged in water; the mass G_2 of the empty basket submerged in water; and the dry mass G_0 of the aggregate after drying. Each apparent density value and its standard deviation are derived from three batch-averaged results. The apparent density was calculated using Equation (1), with results accurate to 10 kg/m^3.

$$\rho_0 = \frac{G_0}{G_0 + G_2 - G_1}\rho_{water} \quad (1)$$

where G_0 is the dry mass of the aggregate after drying (g), G_1 is the total mass of the basket and the specimen submerged in water (g), G_2 is the mass of the empty basket submerged in water (g), and ρ_{water} is 1000 kg/m^3.

2.3.2. Bulk Density

The aggregate was sieved to obtain the 9.5–26.5 mm particle size range. After air-drying, a calibrated 2-L container was filled in three separate batches. After each filling, the container was gently tapped 25 times on a firm surface, alternating between left and right, to compact the material. After filling, the surface was leveled with a steel straight edge so that the volumes of the slightly convex and concave areas were approximately equal. The mass of the container and sample G_3, as well as the mass of the empty container G_4, were weighed. The bulk density given was the average of the three values. Finally, the bulk density was calculated using Equation (2), with the results rounded to the nearest 10 kg/m^3.

$$\rho_1 = \frac{G_3 - G_4}{V} \quad (2)$$

where G_3 is the total mass of the container and sample (g), G_4 is the mass of the empty container (g), and V is the volume of 2-L container (L).

2.3.3. Cylindrical Compressive Strength

The cylindrical compressive strength was tested using a lightweight aggregate compression cylinder, which has a depth of 100 mm and a base diameter of 113 mm. The aggregate was screened to the 9.5–19.0 mm size range, and needle-shaped and flake-shaped non-uniform particles were removed. The sample was divided into three equal portions; one portion was placed into the compression cylinder and tapped to compact it. The cylinder was placed at the center of the universal testing machine platform, and a constant load of 0.5 kN/s was applied until the aggregate was crushed and the compression height reached 20 mm. The load P_2 was recorded. Additionally, the self-weight of

the pressure cylinder (P_1) was measured, and the base area A was calculated geometrically. The reported cylindrical compressive strength was the average of the three values of the test. The cylindrical compressive strength $f_{c\text{-}c}$ of the aggregate was calculated by using Equation (3).

$$f_{c-c} = \frac{P_1 + P_2}{A} \tag{3}$$

where P_1 is the self-weight of the pressure cylinder (kg), P_2 is the force (N) at compression of 20 mm, and A is the base area (mm^2).

2.3.4. Particle Compressive Strength

The air-dried aggregate was screened to obtain the 9.5–26.5 mm size fraction, and relatively regular, nearly spherical particles were selected as test specimens. The long, intermediate, and short axial dimensions were measured using a vernier caliper, and the arithmetic mean diameter d was calculated. A single aggregate particle was placed at the center of a universal testing machine so that the load was transmitted along the principal axis of stress. The specimen was loaded at a constant rate of 0.5 mm/min until failure occurred, and the ultimate load P was recorded. The reported particle compressive strength represented the average of three replicate measurements. The particle compressive strength $f_{c\text{-}p}$ was calculated using Equation (4) [30].

$$f_{c-p} = \frac{2.8P}{\pi d^2} \tag{4}$$

where P is the failure load (N) during crushing of aggregate and d is mean diameter derived from three axial measurements of the aggregate sample (mm).

2.3.5. Porosity Test

Fine particles smaller than 4.75 mm were screened out. Two kg of aggregate in the 4.75–9.5 mm size range was selected and soaked in water for 24 h to reach saturation. The surface moisture was wiped off, and the saturated mass G_5 was measured. Its mass in water G_6 was determined. Subsequently, the samples were dried in an oven at 105 ± 5 °C until a constant weight was achieved, and the mass of the dried samples G_7 was measured. Each porosity was measured on three samples, and standard deviations were reported accordingly. The porosity of aggregate C was calculated using Equation (5).

$$C = \frac{G_5 - G_7}{G_5 - G_6} \times 100\,\% \tag{5}$$

where G_5 is the saturated dry mass of the aggregate (g), G_6 is the mass of the specimen submerged in water (g), and G_7 is the dry mass of the aggregate after drying (g).

2.3.6. Water Absorption Test

The aggregate in the 4.75–9.5 mm size range was taken and soaked in water for 24 h until saturated. The surface moisture was wiped off, and the mass G_5 was weighed. Then, the sample was placed in a drying oven at 105 ± 5 °C until a constant weight was achieved, and the dry mass G_7 was weighed. The water absorption was presented as the mean of three parallel measurements. Finally, the water absorption W was calculated using Equation (6).

$$W = \frac{G_5 - G_7}{G_7} \times 100\,\% \tag{6}$$

where G_5 is the saturated dry mass of the aggregate (g) and G_7 is the dry mass of the aggregate after drying (g).

2.3.7. Freeze-Thaw Resistance Test

To assess the durability of travertine artificial aggregate under freeze–thaw cycles, the freeze–thaw cycling regime (freezing at −20 °C for 4 h and thawing at 20 °C for 4 h) was adopted with reference to GB/T 50082-2009 [31] while the specimen preparation and mass measurement procedures were adapted for testing groups of artificial aggregate particles rather than individual particles, because the standard is primarily intended for concrete/mortar specimens. Aggregate in the 4.75–26.5 mm size range was screened, and after removing surface dust, each group of aggregate was soaked in water at 20 ± 2 °C for 24 h, with the water level at least 20 mm above the specimens; no vacuum saturation was applied. Each group was then removed and gently wiped with a damp cloth until no visible water film remained on the surface. As a special case, the freeze–thaw test was designed differently from the other tests: for each mix proportion, three independent production batches were prepared, and from each batch, 3 kg of recovered 4.75–26.5 mm aggregate was divided into Group A (approximately 1.5 kg, 15 cycles) and Group B (approximately 1.5 kg, 25 cycles). Immediately after grouping, each group was weighed using an electronic balance with a readability of 0.01 g, and each group was weighed as a whole, not as individual particles, and their initial mass (M_0) was recorded. The specimens were frozen at −20 °C for 4 h and then thawed at 20 °C for 4 h, completing one full cycle. After Group A completed 15 cycles, the specimens were removed to observe whether macroscopic damage, such as spalling, cracking, or fragmentation, had occurred on the surface, and their mass (M_1) was measured. Group B continued until 25 cycles were completed, after which the same testing procedure was followed. Upon completion of the test, the mass loss rates of the artificial aggregates before and after freeze–thaw cycles were compared. The mass loss rate ΔM was calculated using Equation (7). For both Group A and Group B, the test was repeated on all three independent batches, and the average of the three batch values was reported separately for 15 and 25 cycles, along with the standard deviations.

$$\Delta M = \frac{M_0 - M_1}{M_0} \times 100\,\% \tag{7}$$

where ΔM is the mass loss rate after the 15th and 25th freeze–thaw cycles (%), M_0 is the initial mass of the aggregate (g), and M_1 is the mass of the aggregate after the 15th and 25th freeze–thaw cycles (g).

2.3.8. SEM Test

The microstructure of the travertine artificial aggregate was characterized by SEM (TM3000, Hitachi, Tokyo, Japan). Representative samples were selected from each group. Surface dust and loose impurities were first removed with anhydrous ethanol, and the samples were then immersed in isopropanol for 24 h to terminate the hydration reaction and replace free water. Afterwards, the samples were dried in an oven at 105 °C for 24 h to remove the residual organic solvents. Prior to observation, the sample surfaces were sputter-coated with a thin gold layer to minimize charging effects and mounted on sample stubs using conductive adhesive. SEM observations were carried out in high-vacuum mode at an accelerating voltage of 15 kV. In addition, it should be noted that drying at

105 °C may partially remove gel water and influence the apparent morphology or stability of certain hydration products, particularly C-S-H gel and ettringite-related phases; therefore, the SEM observations in this study were interpreted primarily in terms of morphological features.

2.3.9. XRD Test

The mineralogical composition of the artificial aggregates was analyzed by XRD. Representative aggregate particles were immersed in isopropanol for 24 h to terminate hydration, dried at 105 °C for 24 h, and then ground into powder. The powder was evenly packed into the sample holder and flattened with a glass slide. XRD patterns were collected using a diffractometer equipped with a Cu anode (Cu Kα radiation, λ = 1.5418 Å) operated at 40 kV and 40 mA. The measurements were performed in locked-coupled mode over a 2θ range of 5–80°, with a step size of approximately 0.052°. Phase identification was carried out by Jade, and quantitative phase analysis was not performed in this study; therefore, the XRD results were used primarily for qualitative identification of the crystalline phases.

3. Results and Discussion

3.1. Porosity

Figure 6 illustrates the trend in the open porosity of artificial aggregates in a system with a high content of travertine powder, reflecting the evolution of the internal structure toward greater density under the synergistic effect of multiple components. G1, as a single-component system, exhibited a low porosity (approximately 19%) at a higher cement content, indicating that this system can form a relatively dense internal structure. This is primarily because a higher cement content provides sufficient hydration products, thereby enhancing interparticle bonding and reducing internal porosity [16]. In contrast, the porosity of the binary system G2 increased to 25%. This is because with a reduced cement content, the system produces fewer hydration products. Fly ash exhibits low reactivity during the early stages of hydration and struggles to participate in reactions in a timely manner to form an effective cementitious structure; therefore, a large number of un-filled pores appear. Consequently, the overall structure of the G2 group was relatively loose, and its porosity was higher.

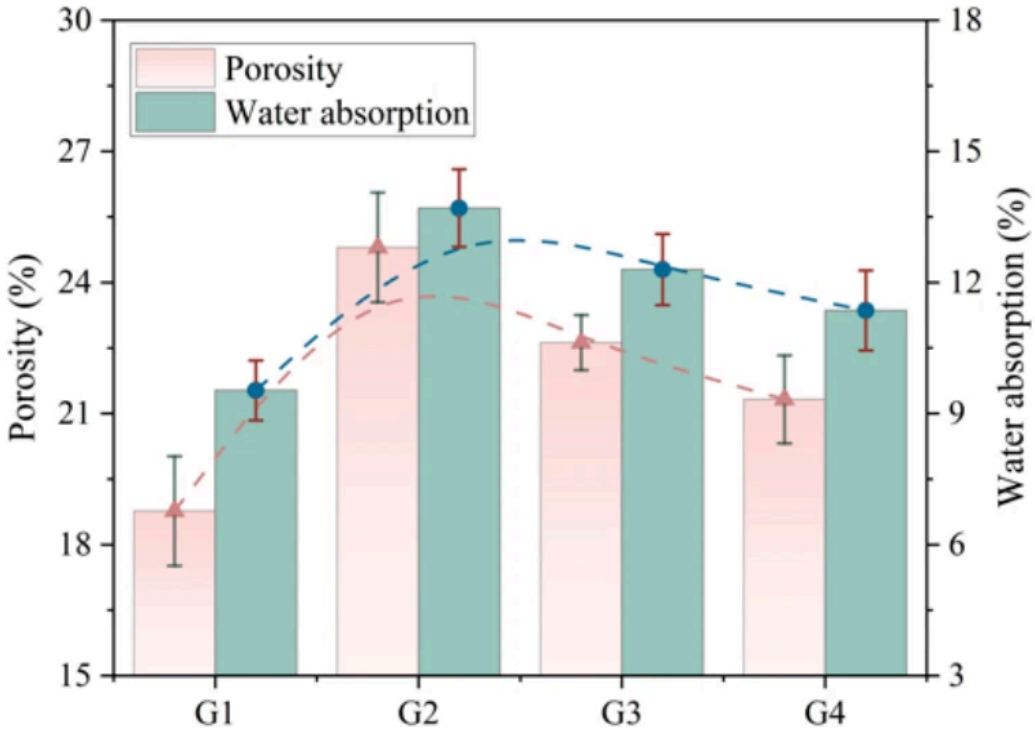


Figure 6. Porosity and water absorption of the travertine artificial aggregates.

In the ternary system, the porosity of G3 showed a decreasing trend compared to G2, falling from 25% to 23%, which suggested that adding a small amount of GGBS might lead to a slightly higher density of the aggregate. This may be because in the alkaline environment formed during cement hydration, GGBS can release active Si and Al components at an early stage, thereby generating C-S-H and some hydration products, such as AFm and AFt, which can fill the capillary pores and thereby improve the interfacial bonding between the travertine particles and the cementitious phase, thereby reducing the system's porosity [18]. In the G4 group, as the GGBS content increased, the aggregate porosity further decreased to 21%, suggesting a trend of further enhanced densification within the aggregate. On the one hand, the increased GGBS content enhances the system's potential reactivity, promoting the formation of more cementitious products [18,32]; on the other hand, the particle size distribution of cement, fly ash, GGBS, and travertine powder forms an optimized particle gradation, allowing fine particles to fill the gaps between larger particles and thereby enhancing the particles' packing density. Therefore, under the influence of various factors, the internal pore structure of the aggregate was further optimized, and the porosity continued to decrease.

3.2. Water Absorption

Figure 6 also shows the changes in the water absorption rate of the aggregates. Overall, the trends in water absorption across the groups generally align with those of porosity. G1 exhibited the lowest water absorption at 10%. This indicates that under conditions of higher cement content, the system can generate a greater amount of hydration products, thereby forming a denser internal structure and more thorough interparticle bonding, which reduces the path through which water can penetrate into the aggregate and results in a lower water absorption rate [16]. These results suggest that the cementitious structure formed by the single-component cement system is relatively complete and effectively suppresses the water absorption behavior of the aggregate. In contrast, G2 exhibited the highest water absorption rate at 14%, indicating that the addition of fly

ash resulted in a relatively loose internal structure. Combined with the porosity results, the structural systems incorporating fly ash not only had an increased total internal porosity, but also a higher proportion of open pores and interconnected capillaries. This allowed water to penetrate the aggregate more rapidly along continuous pathways, leading to an increased water absorption rate of the structure. This is because the reduced cement content weakens early-age setting capacity, while the slow initial reaction of fly ash makes it difficult to effectively fill the pore walls and interface regions in a timely manner, resulting in the aggregate exhibiting a stronger tendency to absorb water. Upon the addition of GGBS, the water absorption rates of both G3 and G4 showed a decreasing trend, which suggests that adding GGBS might lead to slightly higher water resistance. When GGBS is activated in an alkaline environment, it generates more gel products that deposit within the particles and at their interfaces [18,32], thereby blocking and reducing effective water absorption pathways. At the same time, the synergistic filling effect of the multicomponent powder further improves the uniformity of the aggregate's internal structure, making it more difficult for water to penetrate deep into the particles.

3.3. Density

Figure 7 shows the changes in the apparent and bulk densities of the artificial aggregates, and the trends for both are relatively consistent. Unlike porosity and water absorption, apparent density is influenced not only by the internal pore structure but also by the proportion of closed pores in the structure; therefore, it reflects the degree of compactness of the aggregate's internal structure from another perspective. G1 exhibited a higher apparent density of 2424.6 kg/m^3. This indicates that under conditions of higher cement content, the system is able to form a greater amount of hydration products to fill the aggregates' voids, establishing a more complete cementitious matrix and making the aggregate as a whole denser. In contrast, when 15% of the cement was replaced with an equal amount of fly ash, the apparent density of G2 decreased slightly. This is because insufficient early-stage activation in the system caused a delayed reaction of the fly ash, leading to an increase in internal voids within the aggregate and a looser structure. Fly ash primarily exerts a "micro-aggregate filling effect", which resulted in a decrease in apparent density.

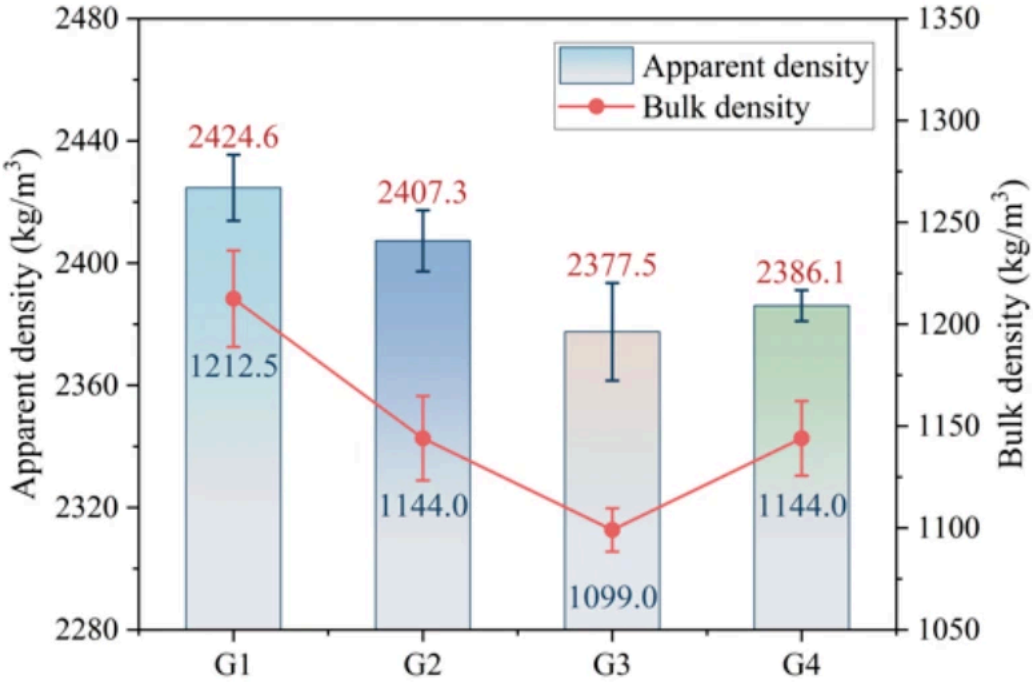


Figure 7. Apparent density and bulk density of the travertine artificial aggregates.

It is worth noting that G3 and G4 exhibit a non-monotonic relationship between porosity and apparent density. Although the porosity decreases from G2 to G4, the apparent density decreases from G2 to G3 and shows a slightly higher value in G4. In this study, the porosity mainly reflects the open pore volume, whereas apparent density is related to the overall mass-to-volume ratio of the aggregate and may also be influenced by closed pores, solid-phase composition, and internal structural uniformity. For G3, the incorporation of 1.5% GGBS may have partially activated the fly ash and refined part of the open pore structure, resulting in a lower porosity than that of G2. However, its effect on the densification of the aggregate remains limited due to the low GGBS content. In G4, the aggregate's apparent density was slightly higher with 4.5% GGBS, suggesting that a higher GGBS content might lead to a trend of improved internal structure of the aggregate. This may be related to the combined effects of GGBS, fly ash, cement, and travertine powder. At this stage, a larger amount of C-S-H and AFt is formed, and their structure is denser [18]. These high-density hydration products not only increase the aggregate's solid mass, but also cause more voids to transform into closed pores, effectively enhancing the aggregate's compactness.

3.4. Compressive Strength

Figure 8 presents the results for the cylindrical and particle compressive strengths of the aggregates. Overall, the trends in these two strength indicators are generally consistent with the results for porosity and water absorption; the denser the aggregate's internal structure and the fewer the pore defects, the better its mechanical properties. In the single-component system, the particle and cylindrical compressive strengths of G1 were 3.04 MPa and 6.23 MPa, respectively. A higher content of cement helps to form a more complete cementitious matrix and enhances the bonding between the travertine particles and the cementitious phase, thereby reducing interfacial defects during compression and enabling the aggregate to exhibit higher compressive strength. In the binary system, G2 exhibited the lowest particle compressive strength, with values of 1.65 MPa and 3.17 MPa for particle and cylindrical compressive strengths, respectively. These results correspond to its higher porosity and water absorption rates, indicating that under conditions of fly ash addition alone, the system's early-stage reaction is insufficient, making it difficult to establish an effective cementitious structure in a timely manner. This leads to more voids and weak interfaces within the aggregate. Under external loading, these defective areas are more prone to cracking, resulting in a notable decrease in particle compressive strength [18].

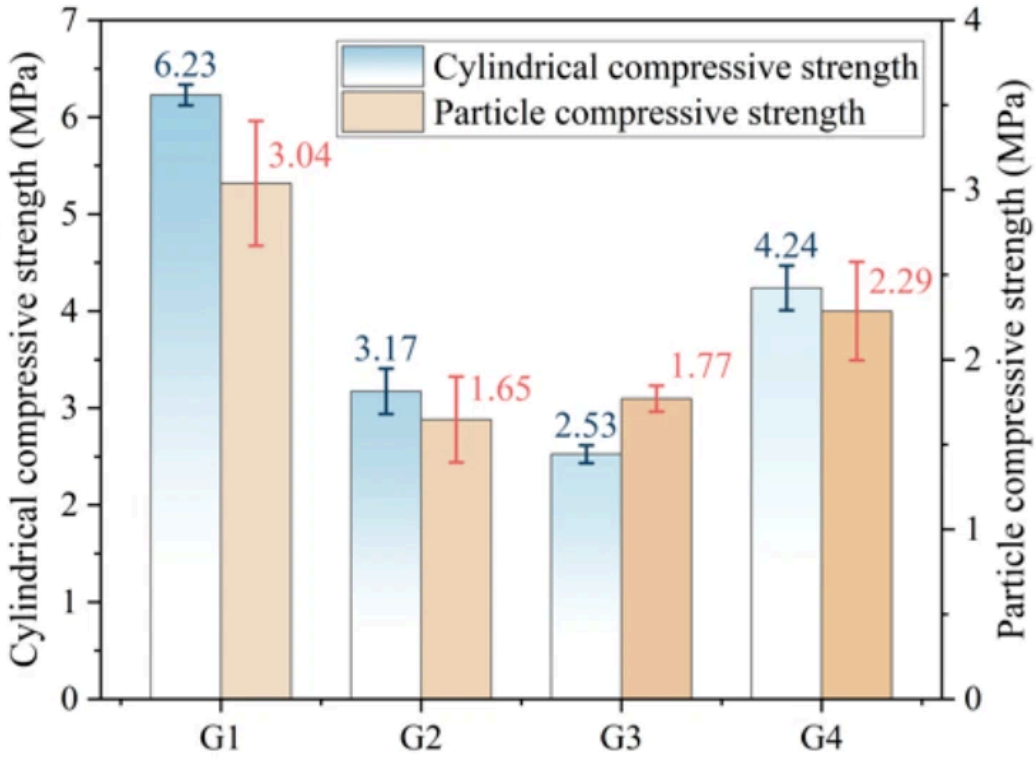


Figure 8. Particle and cylindrical compressive strength of the travertine artificial aggregates.

Upon further incorporation of GGBS, the particle compressive strength exhibited a numerical increasing trend from G2 to G4; specifically, the particle and cylindrical compressive strengths of G4 were slightly higher, reaching 2.29 MPa and 4.24 MPa, respectively. This is because after being activated in an alkaline environment, the GGBS is able to react with the cement to form more cementitious products and improve the interface transition zone structure between the travertine particles and the cementitious materials [32]. At the same time, the synergistic filling effect of the multi-component powder helps to reduce internal pore defects in the aggregate, improving the overall compressive performance of the particles. Although the particle and cylindrical compressive strengths of the G4 group were still 31.9% and 27.8% lower than those of the G1 group, respectively, G4 showed a lower cement content and a higher solid waste substitution rate. Under these conditions, G4 still maintained a relatively substantial compressive strength, indicating that by optimizing the mix design of a multicomponent system, it is possible to achieve good mechanical properties while reducing the cost of cementitious materials and increasing the utilization rate of solid waste. Therefore, the G4 mix design demonstrates a good overall balance between engineering practicality, resource utilization, and environmental benefits, and holds significant potential for engineering applications.

3.5. Relationships Between Properties

In this study, quantitative relationships were established between water absorption (W), porosity (C), particle compressive strength ($f_{c\text{-}p}$), and cylindrical compressive strength ($f_{c\text{-}c}$), as shown in Figures 9–11. The exploratory regression analysis was based on a total of four experimental data points, corresponding to the four binder systems (G1–G4) at 28 days of age. The insets in the corners of the three figures show the relationship between the predicted and measured values of water absorption, porosity, particle and cylindrical compressive strengths for travertine artificial aggregate at 28 days of age, indicating a high correlation between the predicted values from the fitted curves and the experimental values. To provide a complete statistical description, the 95% confi-

dence bands and 95% prediction bands were plotted in the figures, and the coefficient of determination R^2 was reported for each relationship. The functional relationships were initially derived using symbolic regression to identify the optimal physical trends. Based on these derived equations, the slopes were fixed and only the intercepts were fitted. The bands were then calculated using constrained ordinary least squares based on the Student's *t*-distribution ($df = 3$).

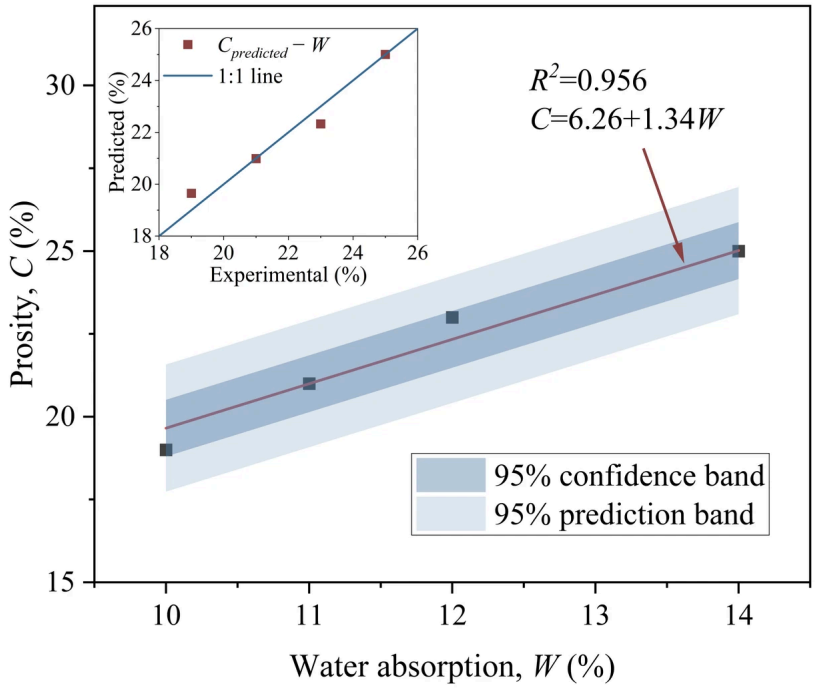


Figure 9. Relationship between water absorption (*W*) and porosity (*C*).

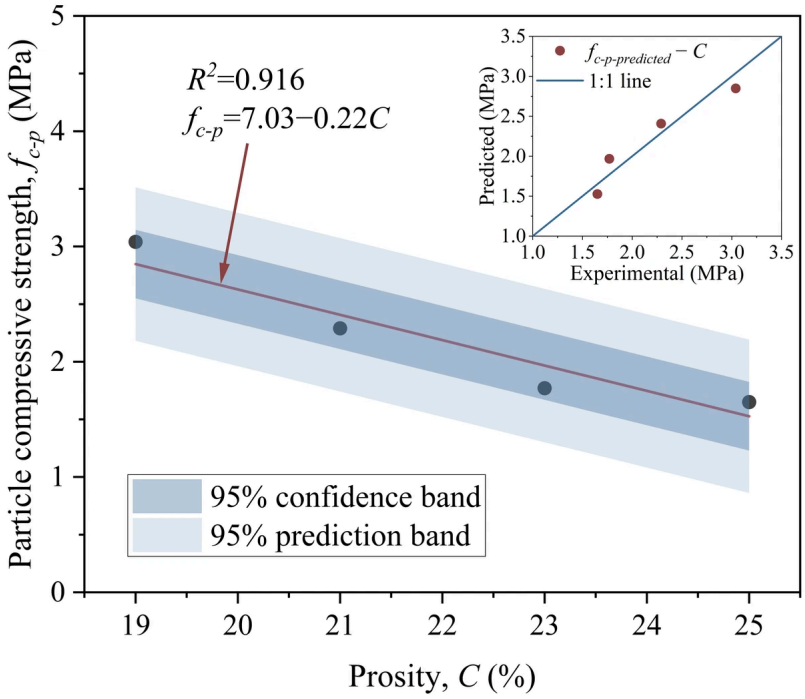


Figure 10. Relationship between porosity (*C*) and particle compressive strength (f_c).

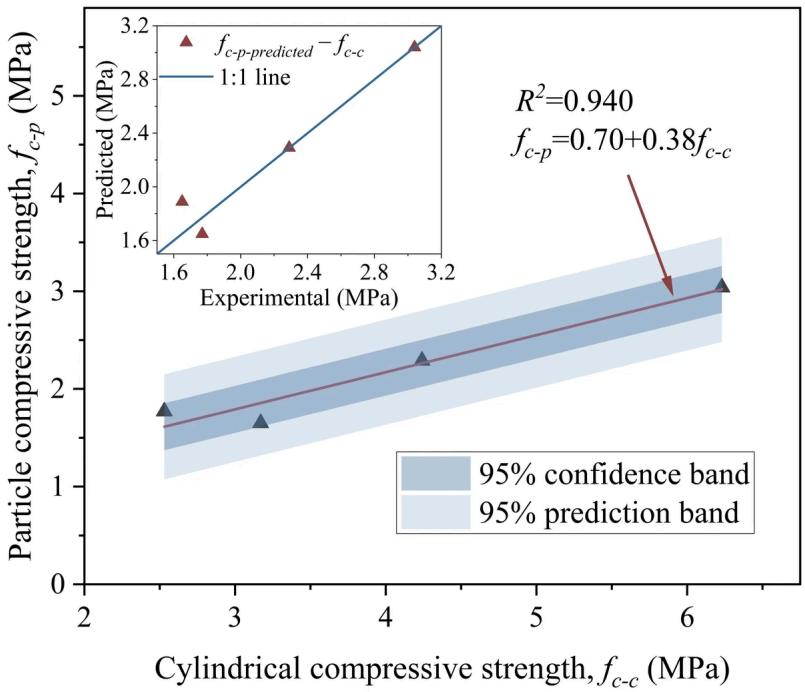


Figure 11. Relationship between cylindrical ($f_{c\text{-}c}$) and particle compressive strength ($f_{c\text{-}p}$).

As shown in Figure 9, the porosity is positively correlated with its water absorption rate; porosity increases as the water absorption rate rises. This is because pores serve as pathways for water to enter the aggregate and as storage spaces for water. The higher

the porosity, the greater the available pathways and storage space for water penetration, and thus the water absorption rate naturally increases. The R^2 value for this relationship is 0.956, as expressed by Equation (8). Figure 10 shows that the 28-day particle compressive strength of the travertine artificial aggregate is negatively correlated with porosity. As porosity increases, particle compressive strength gradually decreases. This is because higher porosity leads to a looser internal structure of the aggregate, reducing the bonding strength between particles and thus lowering the aggregate's ability to resist external forces, with the R^2 value of 0.916, as expressed by Equation (9). From Figure 11, the 28-day cylindrical compressive strength also shows a positive correlation with particle compressive strength; the trends in cylindrical and particle compressive strengths are consistent, both increasing simultaneously. The R^2 value is 0.940, as shown in Equation (10).

The relationships established above are presented strictly as descriptive trends to illustrate the inherent correlations among the investigated properties, rather than as robust predictive models for engineering design. It should be acknowledged that these empirical relationships were derived from a limited dataset of only four data points (G1–G4) and lack independent external validation. Furthermore, because the slopes were derived from the same dataset using symbolic regression and subsequently treated as fixed, this procedure does not adequately account for model-selection uncertainty. While the high R^2 values indicate a strong statistical fit within the investigated range, the low degrees of freedom restrict their reliability, particularly for extrapolation beyond the tested mix proportions. Consequently, the applicability of these equations is restricted to cold-bonded artificial aggregates with high travertine powder content (70%) and similar multicomponent binder systems. Therefore, caution should be exercised when applying them to other material systems, and future studies with larger datasets are required to establish more generalized models.

$$C = 6.26 + 1.34W \tag{8}$$

$$f_{c\text{-}p} = 7.03 - 0.22C \tag{9}$$

$$f_{c\text{-}p} = 0.70 + 0.38f_{c\text{-}c} \tag{10}$$

3.6. Freeze-Thaw Resistance

Freeze-thaw damage to cement concrete involves both the degradation of the matrix at low temperatures and the degradation of the aggregates themselves [32]. To determine the freezing resistance of travertine artificial aggregates, freeze–thaw cycle tests were conducted. Figure 12 shows the mass loss rates of artificial aggregates from different systems. The increase in the number of freeze–thaw cycles led to an increase in the mass loss rate of all sample groups, indicating that repeated freeze–thaw cycles continuously weaken the surface integrity and internal structural stability of the artificial aggregates. Among them, G2 exhibited the greatest mass loss, followed by G3 and G4, while G1 showed the least loss. This difference reveals a close correlation between the aggregate's microscopic pore structure and its macroscopic freeze-thaw durability. G1 exhibited superior freeze-thaw resistance and the lowest mass loss, which is consistent with the dense microstructure revealed above. At high cement content, a sufficient amount of hydration products filled the pores between the travertine particles, resulting in a denser overall structure with lower porosity, thereby conferring a higher freeze-thaw resistance.

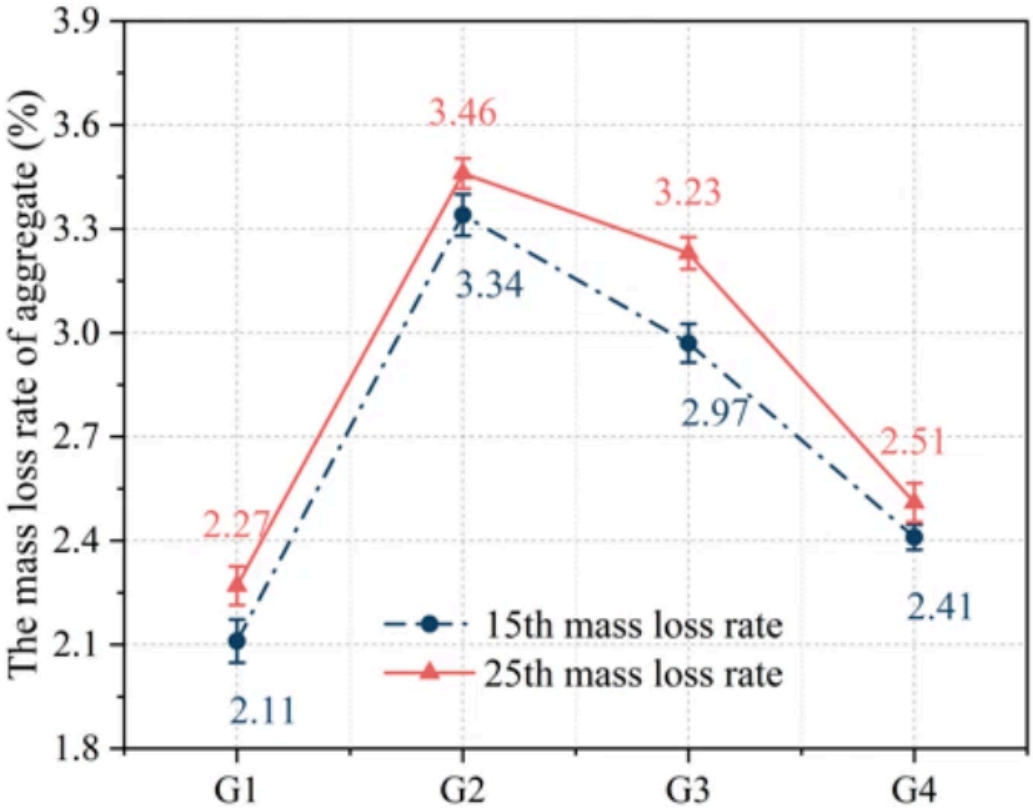


Figure 12. Freeze-thaw resistance of the travertine artificial aggregates.

In contrast, G2 exhibited the highest mass loss and the poorest freeze-thaw resistance. Due to the delayed pozzolanic reaction characteristics of fly ash in the early stages, the matrix pores were not filled in a timely manner, resulting in more interconnected capillary pores within the aggregate and a high content of free water. During the freeze–thaw cycle, the freezing of pore water caused volume expansion, resulting in significant crystalline pressure. Repeated freeze-thaw pressures caused microcracks to continuously form and propagate, ultimately leading to spalling of the aggregate surface and significant mass loss. The mass loss in G3 and G4 showed a slightly lower value than that in G2, which suggests the incorporation of GGBS might lead to an increasing trend in the freeze-thaw resistance of artificial aggregates. This is because the pozzolanic activity of GGBS is activated, allowing it to participate earlier in secondary hydration reactions and form a dense C-S-H gel. These gels effectively filled the interparticle voids, reducing the content of "freezable water" within the system. In G4, which had a higher GGBS content, this densification effect appeared to show a slightly stronger trend.

3.7. SEM Analysis

Figure 13 presents the SEM observations of four groups of the aggregates. It should be noted that the samples were dried at 105 °C for 24 h after solvent treatment, which may have partially removed gel water and affected the apparent morphology of certain hydration products, particularly C-S-H gel and Aft-related phases. Therefore, the following interpretations are based primarily on morphological features and should be considered tentative.

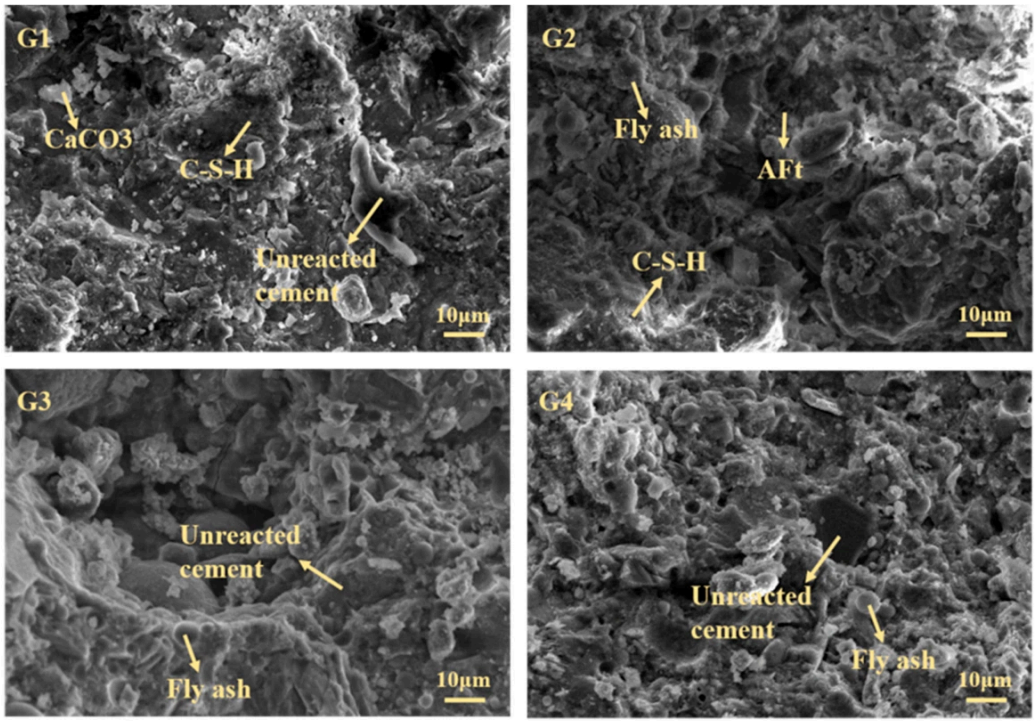


Figure 13. SEM analysis of the travertine artificial aggregates.

In the G1 system, the hydration products appear relatively well-enclosed and the microstructure is comparatively dense, suggesting that the higher cement content contributes to the formation of a more complete cementitious matrix. At the same time, unhydrated cement particles can also be observed locally. In contrast, the microstructure of G2 is relatively loose, with a higher porosity. In G2, spherical fly ash particles surrounded by hydration products are clearly visible, together with acicular and prismatic crystals whose morphology is consistent with AFt phases. Due to the significant time lag of fly ash's pozzolanic reaction, the number of gel-like products, interpreted as C-S-H gel based on morphology, was insufficient to fill the voids between particles and form a continuous, dense cementitious structure [18]. Therefore, the physical and mechanical properties of G2 declined, which is consistent with the previous results on porosity, water absorption, and strength.

The microstructures of G3 and G4 showed a significant improvement compared to G2, with an overall denser structure. Most solid particles were tightly enveloped by hydration products, and the interstitial pores between particles were reduced. At the same time, the boundary between the GGBS particles, which were added in small quantities, and the cement hydration matrix became indistinct. The indistinct boundary may indicate that GGBS may have undergone dissolution and hydration reactions in an alkaline environment; the gel-like products, likely C-S-H, together with the cement hydration products, may fill the tiny pores and improve matrix integrity, thereby improving the mechanical performance of the artificial aggregate [18,32]. A comprehensive comparison of the microstructures of the four sample groups reveals that G1 and G4 exhibit superior density, while G2 is the most porous. The high density of G1 is caused by the large amount of hydration products formed due to the high content of cement, whereas G4 achieved a good level of microstructural density through the synergistic effect of GGBS and fly ash, despite a reduced cement content. This result supports the previously reported test results on the mechanical properties of G4 and confirms the feasibility of a multiple synergistic system for the artificial aggregate substitute. It should be noted that the phase assignments above are based on morphology and are therefore tentative, as

discussed in Section 2.3.8.

3.8. XRD Analysis

Figure 14 presents the XRD patterns of artificial aggregates after they were ground into powder. By studying the typical phases of cement clinker, hydration products, the hydration of fly ash, GGBS, and the minerals in travertine powder, this study investigated the phase composition and reaction characteristics of artificial aggregates in a multi-component system. The XRD patterns show that all four sample groups exhibit distinct diffraction peaks for the $CaCO_3$ phase. This is attributable to the addition of travertine powder, as $CaCO_3$ is the primary crystalline phase in travertine powder. Although the travertine powder content was consistent across all groups, the $CaCO_3$ diffraction peak intensity in the single-component system (G1) was lower than that in the binary and ternary systems. This difference may reflect variations in crystallinity, matrix effects, or sample preparation rather than absolute phase content, and is therefore interpreted qualitatively. Under high cement content, the travertine powder may not only serve as a filler, but may also induce interfacial effects between the particle surfaces and the hydration environment; however, this requires further verification through quantitative characterization or thermal analysis.

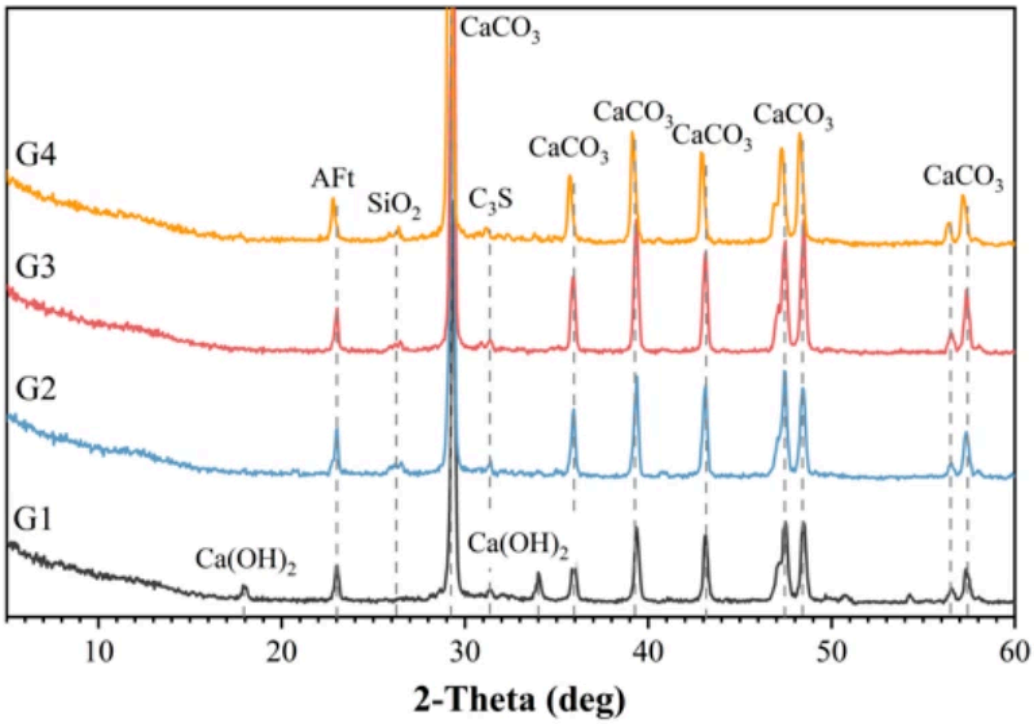


Figure 14. XRD patterns of the travertine artificial aggregates.

Semi-quantitative information can be inferred from the relative intensities of characteristic peaks [33]; however, peak intensity is also affected by crystallinity, preferred orientation, and sample preparation. Therefore, the XRD analysis in this study is qualitative for phase identification, and the peak-intensity comparisons are only semi-quantitative. No Rietveld refinement or internal standard was performed, and the phase contents were not quantified. In the single-component system (G1), a faint $Ca(OH)_2$ characteristic peak can be observed; this $Ca(OH)_2$ is formed as a result of cement hydration. However, in the binary and ternary systems, the $Ca(OH)_2$ characteristic peak weakened or even disappeared with the addition of the GGBS and fly ash. This suggests that the introduction of fly ash and GGBS may have promoted pozzolanic reactions, consuming the

$Ca(OH)_2$ to form more C-S-H gel [18]. The associated formation of additional C-S-H gel is inferred from this trend together with the SEM observations, rather than directly quantified by XRD. It should be noted that C-S-H gel is poorly crystalline and cannot be reliably identified or quantified by conventional XRD; its presence is therefore inferred indirectly from the reduction in $Ca(OH)_2$ peaks and from the SEM observations. In addition, weak diffraction peaks attributable to crystalline SiO_2 were observed in the binary and ternary systems, which may correspond to residual quartz present in the fly ash and GGBS. Diffraction peaks consistent with AFt phases were also observed; however, because AFt content and stability can be affected by sample drying and preparation, these peaks are used here for qualitative phase identification rather than quantitative comparison.

4. Conclusions

This study investigated the feasibility of preparing artificial aggregates using a high content of travertine powder in combination with low contents of cement, fly ash, and GGBS, and the effects of different binder systems on the performance of the artificial aggregates were analyzed. The main conclusions are as follows:

(1) Different bonding systems have a significant impact on the aggregates' pore structure and water absorption. Owing to its relatively high cement content, G1 produced sufficient hydration products and exhibited a comparatively dense internal structure. The cylindrical and particle compressive strengths reached 6.23 MPa and 3.04 MPa respectively, with the lowest water absorption and porosity. Due to the delayed pozzolanic reaction of fly ash, G2 exhibited a relatively loose internal structure, together with higher porosity and water absorption. In G3 and G4, GGBS underwent latent hydration under the alkaline environment, and the generated C-S-H effectively filled its internal pores, thereby reducing both porosity and water absorption.

(2) The incorporation of GGBS was beneficial to the artificial aggregates' mechanical properties and also improved their microstructure. G4 showed the most pronounced improvement. Its cylindrical and particle compressive strengths reached 4.24 MPa and 2.29 MPa, respectively, which were 34% and 39% higher than those of G2, and its water absorption rate and porosity were 16% and 21% lower than those of G2, respectively. The SEM observations further showed that G4 contained more abundant hydration products, exhibited a denser internal structure, and had a more compact interfacial transition zone. In contrast, owing to the relatively insufficient cementitious reaction, G2 contained more internal pores and therefore showed poorer mechanical performance.

(3) The freeze-thaw resistance of the artificial aggregates was closely related to their pore structure. Due to its lower porosity, G1 exhibited the smallest mass loss and the best freeze-thaw resistance. Although G4 contained less cement, the hydration products generated by GGBS improved the structural compactness and reduced the amount of freezable water inside the aggregates. As a result, its freeze-thaw resistance was clearly superior to that of the more porous G2, with the mass loss after 25 cycles decreasing from 3.46% for G2 to 2.51% for G4.

(4) Overall, the GGBS-activated multi-solid-waste cement system can reduce the cement content while improving the pore structure, mechanical properties and freeze-thaw resistance of artificial aggregates. This method offers a new resource utilization approach for the preparation of artificial aggregates from travertine waste, and also provides a reference for the use of related solid-waste materials.

Author Contributions: T.L.: Formal analysis, Investigation, Data curation, Writing—original draft, Writing—review & editing. Y.F.: Investigation, Experiment, Data curation. K.W.: Methodology, Validation. X.T.: Writing—review & editing, Validation. J.X.: Writing—review & editing, Validation. C.Z.: Methodology, Validation. X.M.: Methodology, Validation. B.X.: Investigation, Methodology, Writing—review & editing, Validation. M.L.: Investigation, Writing—review & editing, Validation. All authors have read and agreed to the published version of the manuscript.

Funding: This research received no external funding.

Data Availability Statement: The data presented in this study are available on request from the corresponding author due to subsequent data simulation.

Acknowledgments: Wewould like to acknowledge all of the authors for their valuable help and support in this work.

Conflicts of Interest: The authors declare no conflicts of interest.

References

1. Qi, Y.; Wang, Q.; Li, Z.; Xiong, Y.; Wang, C. Durability and microstructure of bulk solid waste recycled concrete load-bearing block under freeze-thaw cycles. *J. Build. Eng.* **2025**, *112*, 113881. [Google Scholar] [CrossRef]
2. Dong, B.; Yu, Y.; Feng, Y.; Yang, J.; Zhao, G.; Gao, W. Chloride ingress analysis on alkali-activated slag concrete: A validated modelling framework for long-term assessment. *J. Build. Eng.* **2024**, *93*, 109867. [Google Scholar] [CrossRef]
3. Dong, B.; Zhao, S.; Zhang, Y.; Zhang, Y.; Yu, Y.; Yang, J. Physics-based probabilistic analysis of corrosion initiation in alkali-activated slag concrete assisted by machine learning. *Constr. Build. Mater.* **2025**, *471*, 140661. [Google Scholar] [CrossRef]
4. Huang, H.; Zhang, H.; Wu, B.; Bu, J. Development of geopolymer cold-bonded artificial aggregate for UHPC applications based on fresh packing density. *Cem. Concr. Compos.* **2024**, *152*, 105681. [Google Scholar] [CrossRef]
5. Li, C.; Pradhan, P.; Chen, G.; Kropp, J.P.; Schellnhuber, H.J. Carbon footprint of the construction sector is projected to double by 2050 globally. *Commun. Earth Environ.* **2025**, *6*, 831. [Google Scholar] [CrossRef] [PubMed]
6. Liu, J.; Li, Z.; Zhang, W. Research Advances in Cold-bonded Artificial Lightweight Aggregates Made from Industrial Solid Waste Materials. *Mater. Rep.* **2023**, *37*, 131–148. [Google Scholar]
7. Mo, L.; Liu, P.; Xu, M. Carbonation of Steel Slag and Its Application in Producing Low-Carbon Construction Materials. *J. Build. Mater.* **2024**, *27*, 1122–2112. [Google Scholar]
8. Dong, B.; Luo, X.; Tian, K.; Hong, S.; Wang, Y. Preparation and Characterization of Alkali-activated Lithium Slag-based Artificial Aggregates. *Mater. Rep.* **2021**, *35*, 15011–15016. [Google Scholar]
9. Wu, X.; Liu, J.; Guo, W.; Yang, X.; Xue, C.; Zhao, Q.; Dang, W.; Pan, H.; Wang, D. Environmentally friendly artificial aggregates from industrial solid waste: Hydration mechanism and life cycle assessment. *Process Saf. Environ. Prot.* **2025**, *205*, 108198. [Google Scholar] [CrossRef]
10. Kızıltepe, U.; Şahin, Y. Performance assessment of travertine waste as alternative concrete aggregate. *Eur. J. Environ. Civ. Eng.* **2022**, *26*, 7155–7176. [Google Scholar] [CrossRef]
11. Li, T.; Tang, X.; Xia, J. Multi-functional properties of low-carbon travertine aggregate pervious concrete modified by waste limestone powder. *Dev. Built Environ.* **2025**, *21*, 100590. [Google Scholar] [CrossRef]
12. Li, T.; Tang, X.; Xia, J.; Gong, G.; Xu, Y.; Li, M. Investigation of mechanical strength, permeability, durability and environmental effects of pervious concrete from travertine waste material. *Constr. Build. Mater.* **2024**, *426*, 136175. [Google Scholar] [CrossRef]
13. Li, T.; Tang, X.; Xia, J.; Gong, G.; Xu, Y.; Li, M. Investigation of sustainable pervious concrete pavement performance using waste travertine aggregate and powder. *J. Build. Eng.* **2024**, *92*, 109775. [Google Scholar] [CrossRef]
14. Liu, J.; Zheng, W.; Li, Z.; Xie, G.; Cheng, L.; Zhang, W. Research on carbon capture and storage of cold bonded lightweight aggregate from incineration bottom ash. *Constr. Build. Mater.* **2025**, *496*, 143777. [Google Scholar] [CrossRef]
15. Liu, F.; He, Y.; Liu, J.; Zhang, F.; Hao, X.; Liu, C. Performance Research of Ultra-High Performance Concrete Incorporating Municipal Solid Waste Incineration Fly Ash. *Materials* **2025**, *18*, 4623. [Google Scholar] [CrossRef] [PubMed]
16. Narattha, C.; Chaipanich, A. Phase characterizations, physical properties and strength of environment-friendly cold-bonded fly ash lightweight aggregates. *J. Clean. Prod.* **2018**, *171*, 1094–1100. [Google Scholar] [CrossRef]
17. Pan, H.; Si, X.; Wang, S.; Wang, J.; Bao, K.; Zhao, Q. Preparation of low-carbon and environmentally friendly non-sintered ceramsite (NSC) employing steel slag, GGBS and fly ash: Experiment and performance regulation. *Constr. Build. Mater.* **2024**, *411*,

134438. [Google Scholar] [CrossRef]
18. Zhang, Z.; Lyu, J.; Liu, S.; Ma, S.; Zhang, Z.; Niu, X.; Wang, C.; Zhou, C.; Song, L.; Ma, K.; et al. Preparation of artificial aggregates with high fly ash content through air curing and carbonation curing. *Constr. Build. Mater.* **2025**, *461*, 139874. [Google Scholar] [CrossRef]
19. Ma, W.; Li, Z.; Li, C.; Zhang, L.; Li, M. Preparation of Calcined-Free Artificial Aggregate from Phosphogypsum and Its Performance. *J. Build. Mater.* **2024**, *27*, 375–380. [Google Scholar]
20. Shang, X.; Huang, W.; Fang, Z.; Chen, Y.; Zhang, B. Preparation and properties of artificial cold-bonded lightweight aggregate high-strength concrete. *Acta Mater. Compos. Sin.* **2025**, *42*, 1010–1020. [Google Scholar]
21. Tian, K.; Wang, Y.; Hong, S.; Zhang, J.; Hou, D.; Dong, B.; Xing, F. Alkali-activated artificial aggregates fabricated by red mud and fly ash: Performance and microstructure. *Constr. Build. Mater.* **2021**, *281*, 122552. [Google Scholar] [CrossRef]
22. Tekin, I. Properties of NaOH activated geopolymer with marble, travertine and volcanic tuff wastes. *Constr. Build. Mater.* **2016**, *127*, 607–617. [Google Scholar] [CrossRef]
23. Shishegaran, A.; Saeedi, M.; Mirvalad, S.; Korayem, A.H. The mechanical strength of the artificial stones, containing the travertine wastes and sand. *J. Mater. Res. Technol.* **2021**, *11*, 1688–1709. [Google Scholar] [CrossRef]
24. Li, T.; Xia, J.; Tang, X. Effect of eco-friendly pervious concrete pavement with travertine waste and sand on the heavy metal removal and runoff reduction performance. *J. Environ. Manag.* **2024**, *366*, 121757. [Google Scholar] [CrossRef] [PubMed]
25. Shen, P.; Lu, J.; Zheng, H.; Liu, S.; Poon, C.S. Conceptual design and performance evaluation of high strength pervious concrete. *Constr. Build. Mater.* **2021**, *269*, 121342. [Google Scholar] [CrossRef]
26. Ma, Y.; You, Q.; Li, J.; Lu, C.; Yin, J.; Li, H.; Meng, W.; Liu, Z.; Wang, Y.; Gao, X.; et al. Study on the use of CO2 to strengthen recycled aggregates and pervious concrete. *Constr. Build. Mater.* **2024**, *418*, 135372. [Google Scholar] [CrossRef]
27. Shrestha, A.R.; Xia, J.; Di Sarno, L.; Chin, C.S. Feasibility study of utilizing Autoclaved Aerated Concrete (AAC) waste for the production of cold bonded lightweight artificial aggregate using high volume fly ash (HVFA) binders. *Constr. Build. Mater.* **2024**, *449*, 138414. [Google Scholar] [CrossRef]
28. Li, S.; Shao, Y.; Ma, S.; Wang, J.; Zhang, Z.; Liu, X.; Sun, Y.; Zhu, L.; Han, C. Early-age mechanical properties and hydration mechanism of red mud-fly ash-ground granulated blast furnace slag-based steam-cured concrete. *Constr. Build. Mater.* **2025**, *495*, 143617. [Google Scholar] [CrossRef]
29. *GB/T 14685-2011*; Pebble and Crushed Stone for Construction. China Standard Press: Beijing, China, 2011.
30. Li, Y.; Wu, D.; Zhang, J.; Chang, L.; Wu, D.; Fang, Z.; Shi, Y. Measurement and statistics of single pellet mechanical strength of differently shaped catalysts. *Powder Technol.* **2000**, *113*, 176–184. [Google Scholar] [CrossRef]
31. *GB/T 50082-2009*; Standard for Test Methods of Long-Term Performance and Durability of Ordinary Concrete. China Building Industry Press: Beijing, China, 2009.
32. Huang, J.; Hou, J.; Zheng, P.; Wang, J.; Tao, W.; Duan, G.; Zhang, X. Preparation and Properties of Fly Ash-Ground Granulated Blast Furnace Slag Based Artificial Lightweight Aggregate. *Mater. Rep.* **2024**, *38*, 150r–158r. [Google Scholar]
33. Liu, M.; Liu, E.; Hao, J.L.; Di Sarno, L.; Xia, J. Hydration and material properties of blended cement with ground desert sand. *Constr. Build. Mater.* **2023**, *389*, 131624. [Google Scholar] [CrossRef]

Disclaimer/Publisher's Note: The statements, opinions and data contained in all publications are solely those of the individual author(s) and contributor(s) and not of MDPI and/or the editor(s). MDPI and/or the editor(s) disclaim responsibility for any injury to people or property resulting from any ideas, methods, instructions or products referred to in the content.